The Astrophysical Journal, 908:5 (14pp), 2021 February 10 https://doi.org/10.3847/1538-4357/abd724

On the Rigidity Spectrum of Cosmic-Ray Variations within Propagating Interplanetary Disturbances: Neutron Monitor and SOHO/EPHIN Observations at ∼1–10 GV

Anatoly Belov[1], Athanasios Papaioannou[2], Maria Abunina[1], Mateja Dumbovic[3], Ian G. Richardson[4,5], Bernd Heber[6], Patrick Kuhl[6], Konstantin Herbst[6], Anastasios Anastasiadis[2], Angelos Vourlidas[2,7], Eugenia Eroshenko[1], and Artem Abunin[1]

[1] Pushkov Institute of Terrestrial Magnetism, Ionosphere and Radio Wave Propagation of Russian Academy of Sciences (IZMIRAN), 108840, Moscow Troitsk, Russia

[2] Institute for Astronomy, Astrophysics, Space Applications and Remote Sensing (IAASARS), National Observatory of Athens, I. Metaxa & Vas. Pavlou St., 15236 Penteli, Greece; atpapaio@astro.noa.gr

[3] Hvar Observatory, Faculty of Geodesy, University of Zagreb, Kaciceva 26, HR-10000, Zagreb, Croatia

[4] Heliophysics Division, NASA Goddard Space Flight Center, Greenbelt, MD 20771, USA

[5] Department of Astronomy, University of Maryland, College Park, MD 20742, USA

[6] Department of Extraterrestrial Physics, Christian-Albrechts University in Kiel, Liebnitzstrasse 11, D-24098, Kiel, Germany

[7] The Johns Hopkins University Applied Physics Laboratory, Laurel, MD 20723, USA

Received 2020 November 7; revised 2020 December 15; accepted 2020 December 27; published 2021 February 8

Abstract

The rigidity dependence of all Forbush decreases (FDs) recorded from 1995 to 2015 has been determined using neutron monitor (NM) and Solar and Heliospheric Observatory (SOHO) (EPHIN) spacecraft data, covering the energy (rigidity) range from ∼433 MeV (1 GV) to 9.10 GeV (10 GV). We analyzed a total of 421 events and determined the spectrum in rigidity with an inverse power-law fit. As a result, the mean spectral index was identified to be $\langle\gamma_F\rangle = 0.46 \pm 0.02$. The majority (∼66%) of the FDs have γ_F within the range 0.3–0.7. The remaining one-third of the events (∼33%) have either (very) soft or hard FD spectra, with the latter being more common than the former. Significant variations of γ_F occur within almost every FD event. During the initial FD decay phase the spectrum becomes gradually harder, in contrast to the recovery phase, when it becomes softer. Additionally, low energies (rigidities) seem to be better suited for studying the fine structure of interplanetary disturbances (primarily interplanetary coronal mass ejections) that lead to FDs. In particular, FDs recorded by the EPHIN instrument on SOHO better capture a *two-step* structure than FDs observed by NMs. Finally, the ejecta of an ICME, especially when identified as a *magnetic cloud*, often leads to abrupt changes in the slope of γ_F.

Unified Astronomy Thesaurus concepts: Solar coronal mass ejections (310); Forbush effect (546); Corotating streams (314)

Supporting material: machine-readable table

1. Introduction

Galactic cosmic rays (GCRs) are high-energy charged particles accelerated outside our solar system that penetrate the heliosphere, filling interplanetary (IP) space. When GCRs enter the heliosphere, they interact with the interplanetary magnetic field (IMF) (Owens & Forsyth 2013), which is dragged out from the Sun by the solar wind (SW). Rotation of the Sun twists the IMF into an Archimedean spiral configuration, often called a ”Parker spiral” (Parker 1965). The GCRs are scattered by irregularities in the IMF, undergo convection and adiabatic deceleration in the expanding SW, and experience gradient and curvature drifts in the large-scale IMF (Parker 1958). As a result, their intensity is modulated on timescales that vary from millennia (McCracken et al. 2013) to the 22 yr solar Hale cycle (Thomas et al. 2014) and the 11 yr solar cycle (Belov 2000), and, of interest here, to hours to a few days. Such short-term depressions in the GCR intensity were identified by Forbush (1938)—and also by Hess & Demmelmair (1937), who noted that they were often closely associated with geomagnetic storms and were observed worldwide. Such short-term GCR depressions are generally referred to as “Forbush decreases” (FDs). GCR modulations that recur at the solar rotation period were also identified (e.g., Monk & Compton 1939).

It is now well established that such short-term GCR modulations are associated with large structures propagating in the IP medium. In particular, high-speed streams that emanate from coronal holes at the Sun, and the corotating interaction regions (CIRs) that form as they interact with the preceding slower solar wind (see Richardson 2018 for a recent review), give rise to recurrent modulations. In addition, FDs are clearly caused by the passage of interplanetary coronal mass ejections (ICMEs) (e.g., Cane 2000; Belov 2009; Dumbović et al. 2020; Light et al. 2020; Papaioannou et al. 2020 and references therein). The FD often commences at the passage of the shock (if present) upstream of the ICME, and the GCR intensity may further decrease in the ICME. Adding to this, if the ICME contains enhanced magnetic fields that rotate slowly through a large change in direction, it may be classified as a “magnetic cloud” (MC) (Klein & Burlaga 1982). MCs can strongly modulate GCRs (e.g., Richardson & Cane 2011; Belov et al. 2015; Masías-Meza et al. 2016).

For the past 60 years, neutron monitors (NMs) have recorded the variation of GCRs at Earth including FDs (e.g., Lockwood 1971; Papaioannou et al. 2010; Dumbović et al. 2012). GCRs have also been observed by spacecraft both near Earth and at other locations in the heliosphere. However, restrictions on the size and mass of spacecraft instruments usually constrain the energy range of the GCRs detected (often limited to a few hundred MeV) and their counting statistics. An exception to this is the Ulysses Kiel Electron Telescope (KET) described in Simpson et al. (1992), which was designed to measure the electrons in the range from 2.5 to above 150 MeV, and protons

Table 1
A Sample of the List of FDs Recorded at EPHIN on board SOHO from 1995 to 2015

No.	Date	Time	A_S (%)	A_E (%)	γ_F	σ_F	Type of Structure	Two-step FD	
								@ EPHIN	@ NMs at 10 GV
1	1995.12.15	15:15	2.04	0.8	0.53	0.19	ICME	0	0
2	1995.12.24	6:00	3.14	1.5	0.43	0.12		0	0
3	1996.04.08	13:34	2.91	0.5	0.94	0.17		1	0
4	1996.06.19	2:45	0.98	0.6	0.29	0.38		0	0
5	1996.07.01	13:20	1.89	0.7	0.18	0.19	ICME	1	1
6	1996.07.28	13:07	2.06	1.1	0.37	0.18		1	0
7	1996.08.07	12:00	2.69	0.8	0.12	0.14	ICME	1	1
8	1996.08.12	22:34	1.23	0.7	0.33	0.31		0	0
9	1996.09.03	18:00	7.75	2.7	0.59	0.05		1	1
10	1996.09.09	19:13	4.5	0.8	0.92	0.11		1	1
11	1996.11.11	15:27	0.8	0.5	0.28	0.48		0	0
12	1996.11.13	13:00	2.92	1.1	0.55	0.14		0	0
13	1996.12.02	10:01	3.73	1.1	0.67	0.11	ICME	1	1
14	1997.01.10	1:04	2.84	1.1	0.54	0.14	ICME	0	0
15	1997.01.11	1:16	1.23	1.2	0.02	0.3	CIR+ICME	1	1
16	1997.02.09	13:21	6.52	1.5	0.8	0.07	ICME	1	1
17	1997.03.05	13:57	0.6	0.9	−0.26	0.6		0	0
18	1997.03.23	8:23	0.96	0.5	0.38	0.4		0	0
19	1997.04.04	17:45	0.95	0.5	0.37	0.4		1	0
20	1997.04.10	12:58	12.37	3.7	0.67	0.03	ICME	1	0

Note. Column 1 provides the number of the event, columns 2 and 3 the date and onset time of the FD, column 4 the amplitude of the FD by EPHIN (A_S), column 5 the magnitude of the FD by NMs (A_E), column 6 γ_F, column 7 σ_F, column 8 the type of structure; columns 9 and 10 indicate whether a two-step FD was identified at EPHIN or at NMs respectively (1 = yes, 0 = no).

(This table is available in its entirety in machine-readable form.)

and helium from 4 MeV/nucleon to above 2 GeV/nucleon, respectively. Proton and helium fluxes in the energy range from 250 MeV/nucleon to 2 GeV/nucleon have been extensively used to investigate the recurrent modulations caused by CIRs along the Ulysses trajectory (see Kunow et al. 1995). The rigidity dependence of the strongest recurrent FDs and a comparison between solar cycles 22 and 23 were presented in Paizis et al. (1999) and Dunzlaff et al. (2008), respectively. Another exception to the limited energy response is the PAMELA instrument (Adriani et al. 2009), which detects GCRs from 80 MeV to several GeV. An FD observed by PAMELA is reported by Munini et al. (2018). In addition, the Alpha Magnetic Spectrometer (AMS) on the International Space Station (Aguilar et al. 2015) has also observed FDs to at least ∼10 GV (Consolandi & AMS Collaboration 2015). As a notable example of spacecraft observations of GCRs away from Earth, the Voyager 1 and 2 spacecraft observed GCRs as they moved out through the heliosphere, including FDs (e.g., Webber et al. 2007). Paularena et al. (2001) investigated the evolution of an ICME and corresponding FD from the inner heliosphere to beyond 58 au.

Another approach is to use the counting rate of an element of a spacecraft instrument that detects GCRs either as a background or intentionally, as in the case of an anticoincidence shield. Although the counting statistics may be higher, the energy/rigidity response is usually poorly defined since GCRs of a wide range of energies are detected. In addition, solar energetic particles (SEPs) below GCR energies can also be detected and may occasionally dominate the counting rate (e.g., Dumbović et al. 2020). As examples of such observations, McCracken et al. (1966) detected recurrent GCR modulations with a CsI scintillator on Pioneer 6, in a heliocentric orbit ∼50° longitude from Earth, which recorded ∼56,000 counts/7.5 minutes. Cane et al. (1994) used anticoincidence guard rates from instruments on IMP 8 at Earth and the Helios spacecraft to examine FDs associated with ICMEs and shocks in the inner heliosphere, while Richardson (2004) discusses observations of recurrent FDs using the same instrumentation. Adding to this, Blanco et al. (2013) investigated cosmic-ray decreases that were associated with the passage of MCs that were measured by the guard counter of the Helios E6 experiment. The anticoincidence shield (ACS) of INTEGRAL's spectrometer has also been used for FD studies (Jordan et al. 2011). Other near-Earth measurements of FDs include those from the Electron Proton Helium Instrument (EPHIN) instruments on board the Solar and Heliospheric Observatory (SOHO), which will be used in this study, and Chandra (Heber et al. 2015; Dumbović et al. 2018, 2020). Observations beyond Earth include: at Mars, the Radiation Assessment Dosimetry dose rates on the Mars Science Laboratory (Guo et al. 2018; Papaioannou et al. 2019; Freiherr von Forstner et al. 2020); at Saturn, measurements from Cassini's Magnetosphere Imaging Instrument/Low Energy Magnetospheric Measurement System (Roussos et al. 2018); and beyond (e.g., Witasse et al. 2017; Winslow et al. 2018).

In this work, we study short-term modulations of GCRs (i.e., FDs) using observations made by NMs on Earth and by EPHIN on board SOHO at L1 during 1995–2015, extending over solar cycles 23 and 24. We first create a catalog of FDs recorded by EPHIN (a portion of which is presented in Table 1 for guidance regarding its form and content, while the complete table is available in a machine-readable form in the online journal), and then investigate the rigidity dependence of the amplitude of the FDs measured by EPHIN, with a peak response to GCRs at ∼1–1.5 GV, and at 10 GV based on NM observations. We aim at revealing features of the rigidity spectrum, in an attempt to understand the observed variability of FDs.

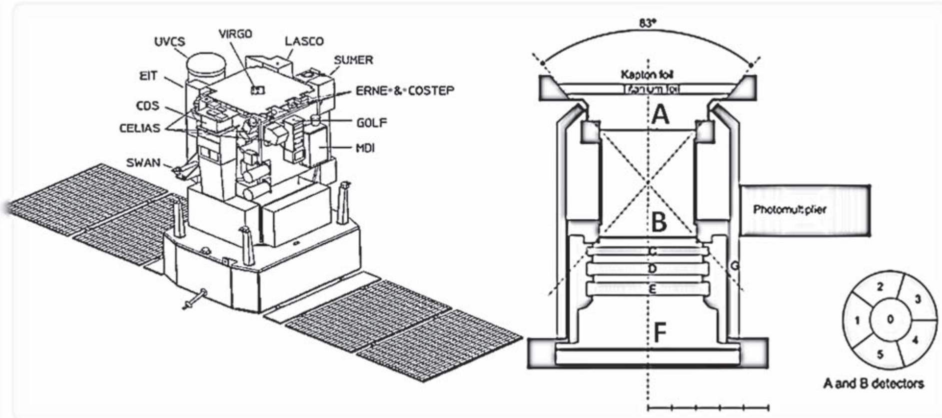

Figure 1. SOHO (left) with the position of COSTEP, which includes EPHIN, and a sketch of the EPHIN detector (right), adapted from Kühl et al. (2015).

2. Analysis

2.1. Data Used

Data on FDs and IP disturbances have been compiled into a database (Forbush effects[8] and interplanetary disturbances—FEID; http://spaceweather.izmiran.ru/eng/dbs.html) by the IZMIRAN Cosmic Ray Group. This is based on the database of variations of cosmic rays (VCR) that was first constructed and transferred into open access at http://spaceweather.izmiran.ru/eng/vcr.html. The VCR database includes hourly values of the basic parameters of cosmic rays at a fixed rigidity of 10 GV—in particular, the variations of CR density (A_0), which is used in this work, and the components of the 3D CR anisotropy (A_x, A_y, A_z) above the Earth's atmosphere and magnetosphere, derived by the global survey method (GSM) (Belov et al. 2018). GSM is applied to the data of the worldwide neutron monitor network (i.e., www.nmdb.eu), taking into account the unique properties of each station such as coupling coefficients, asymptotic directions, and yield functions (Asipenka et al. 2009). It should be noted that the derived cosmic-ray parameters are global characteristics and do not depend on individual NMs. In addition, the VCR database contains hourly information for more than 60 yr and covers the period from 1957 July to 2019 December. As a result, this database is the largest and most comprehensive source of data on CR variations. From the VCR data, Forbush decreases are selected and their solar sources are identified. These results, together with all relevant data and outputs are stored in the FEID database. FEID further includes the hourly IP data from the OMNI database; the list of sudden storm commencements (SSCs) from http://isgi.unistra.fr/data_download.php, CME identifications from https://cdaw.gsfc.nasa.gov/CME_list/, and the solar flares associated with the FDs reported in the solar geophysical data (ftp://ftp.swpc.noaa.gov/pub/indices/events/) as well as in the GOES X-ray list (https://www.ngdc.noaa.gov/stp/space-weather/solar-data/solar-features/solar-flares/x-rays/goes/xrs/). The FEID database also includes all relevant IP data and geomagnetic indices (Kp, Dst). In order to pinpoint the characteristics of the recorded FDs (e.g., magnitude, decrement, 3D anisotropy) we use the results of GSM (Belov et al. 2018). The FEID catalog is based on the density of CR variations (isotropic component of the CR variations, A_0) at a fixed rigidity of 10 GV. These FDs are not limited in size and duration and are often very small (about 0.3%) (Belov et al. 2001). Analysis of the neutron monitor network data by GSM gives an accuracy of ∼0.05%–0.06% (see, e.g., Belov et al. 2018 for details), making it possible to identify such small FDs (Belov 2009). The main requirement for an FD to be included in the FEID catalog is that the observed CR variations are associated with a large-scale SW disturbance. As a result, FEID includes all identified decreases in the GCR density and has more than 7500 FDs that are driven by shocks, ICMEs, CIRs, and combinations thereof. Thus, it provides a large sample of events for FD studies.

Additionally, we utilized measurements from EPHIN, which is part of the Comprehensive Suprathermal and Energetic Particle Analyzer (COSTEP) suite (Müller-Mellin et al. 1995) on board SOHO. SOHO was launched in 1995 December and has an orbit around the Lagrangian point L1. Figure 1 (left) shows a sketch of SOHO with the position of all relevant instruments indicated including COSTEP. The diagram on the right shows EPHIN, which consists of six solid-state detectors (labeled A–F) enclosed in a scintillator that acts as an anticoincidence shield (G). EPHIN was designed to measure ions from 4 to above 50 MeV/nucleon in four coincidence channels for particles stopping in the detector stack, as well as an integral channel (Kühl et al. 2017; Kühl & Heber 2019). In this work, we make use of detector F, which was chosen for this study since it is less sensitive to low-energy particles (i.e., not every soft SEP event will trigger it) than the anticoincidence shield G. Both the F and G detectors can be used to study FDs, but although G has count rate about twice that of F, it also detects more solar particle events. Furthermore, the F detector and a typical NM at the pole have a counting rate of more than 1000 counts/minute (Moraal et al. 2000; Kühl et al. 2015), providing sufficient statistics to observe structures in FDs at even a resolution of a minute (Dumbović et al. 2020).

2.2. Details of the EPHIN Detector

In order to accomplish the study, it is necessary to determine the contribution of particles of different energies (rigidities) to the counting rate of the EPHIN F detector. The geometrical factor of the F detector as a function of CR energy is calculated in Kühl et al. (2015) and is presented in Figure 2. The mounting location

[8] Forbush effects are the broader definition of Forbush decreases; see Belov (2009) for details.

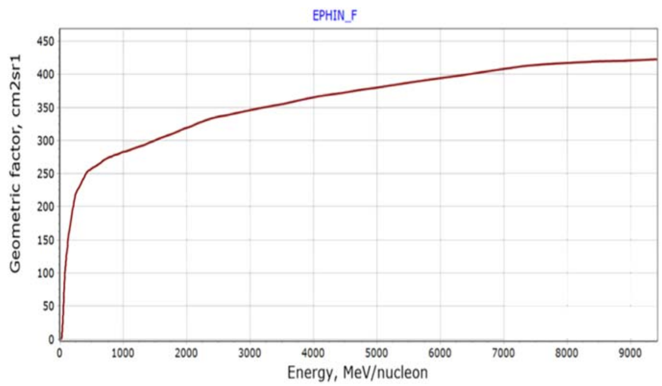

Figure 2. The dependence of the sensitivity of the F detector of EPHIN on CR particles of different energies.

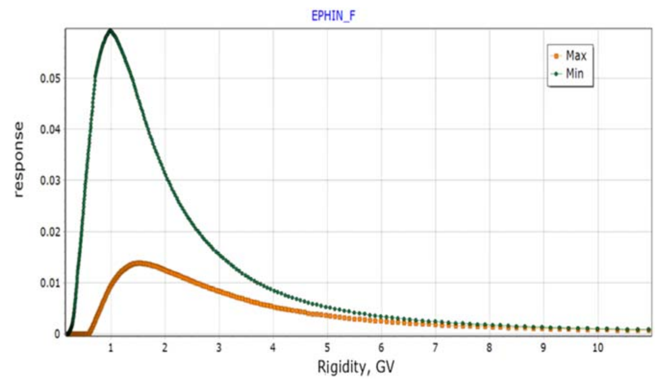

Figure 3. The response function of the EPHIN F detector to CRs with rigidity spectra corresponding to the minimum (2009) (green line) and maximum (2003 November) (brown line) of solar activity.

on SOHO (Figure 1) leads to inhomogeneities in the material encountered by the incoming particles, which depends on their direction of incidence. This has been estimated as equivalent to ~10 cm aluminum mounted behind the sensor. As a result, forward particles only need to penetrate the upper parts of the instrument (e.g., detectors A–E), while backward particles need to penetrate much more material. The detector itself cannot distinguish between these populations coming from the forward or the backward direction. As a result, the response depends on direction. As shown in Figure 1 of Kühl et al. (2015), which was constructed utilizing GEANT-4 simulations, the F detector is sensitive to forward ions >50 MeV and backward ions >150 MeV. Although there are uncertainties in such simulations, the detector configuration employed in this study has been successfully used for the recreation of the GCR modulation (Kühl et al. 2015). Furthermore, results of the EPHIN simulation for penetrating particles have been verified versus AMS-02, PAMELA, and BESS measurements (Kühl et al. 2016). As a result, the GEANT-4 MC uncertainty is likely to be small.

The efficiency $E_F(E)$ of the F detector increases rapidly in the low-energy region (approximately up to 500 MeV), then more slowly with increasing energy. To get the contribution of particles of different energies (rigidities) to the detector counting rate (i.e., response function), it is necessary to multiply the detector efficiency by the primary energy (rigidity) differential spectrum. The CR variation observed by EPHIN can be written as

$$\delta(t,\, t_b,\, R) = \frac{\int_{R_d}^{R_u} \delta_0(t,\, t_b,\, R) W(t_b,\, E(R)) \frac{\partial E}{\partial R} dR}{\int_{R_d}^{R_u} W(t_b,\, E(R)) \frac{\partial E}{\partial R} dR} \qquad (1)$$

where $\delta_0(t,\, t_b,\, R)$ is the variation of the primary CRs, which depends not only on the time t and the rigidity R, but also on the base period t_b. The response function $W(R)$ also depends on the choice of the base period t_b, and this dependence is stronger for the particles of lower energy (rigidity). As a result, it is much more important for satellite observations (e.g., EPHIN) to account for this dependence than for ground-based ones (e.g., NMs). To take into account these changes, we used the information on long-term variations of the CR rigidity spectrum obtained from Gushchina et al. (2012).

An optimal candidate period for the primary spectrum lies in the minima of solar activity, when the CR intensity changes at a slower rate than at other phases of the solar cycle. In this work, we utilized the response function $W(E) = E_F(E)J_{2009}(E)$, using as basis the year 2009. In that particular year, from the time span covered in our study, the CR intensity was the highest recorded for both NMs and EPHIN (which is clearly seen in Figure 4). Evidently, such a reference base period and the corresponding response functions are convenient for the investigation of long-term CR variations (Gushchina et al. 2012, 2013). However, FDs are short-term changes of the background CRs. Therefore, for each event, these changes need to be determined for a new (evolving with time) base and for the corresponding response function, taking into account changes in the primary spectrum (modulation).

Figure 3 shows the difference in the sensitivity of the detector (response function) for the minimum (2009; green line) and maximum of solar activity[9] (2003 November; orange line). It can be seen that at the minimum of solar activity, the maximum sensitivity of the detector is ~1 GV, and at the maximum of solar activity, it shifts to ~1.5 GV. At the minimum of solar activity, the detection range extends to lower rigidities, and the sensitivity to high rigidity significantly increases. Furthermore, the maximum of solar activity (in terms of the number of sunspots) was reached in 2000 with a second peak in 2001. The GCR remained low until the end of 2003. The lowest absolute GCR flux was reached during the largest FD, in 2003 October, which was followed by a series of strong FDs in 2003 November. Thus, we have chosen 2003 November for the calculation of the sensitivity of the detector (response function) for the maximum of solar activity. If we represent the primary variation as an inverse power law in rigidity, i.e., $\delta_0(t,\, t_b,\, R) = A_{\rm E}(R/10)^{-\gamma}$, and substitute it in Equation (1) for $\delta(t,\, t_b,\, R)$ to the $A_{\rm S}$ magnitude (i.e., the FD magnitude at SOHO/EPHIN), and consequently substitute the specific values of $A_{\rm E}$ and $A_{\rm S}$ from the data, then from their relation with Equation (1) we can find an index of the rigidity spectrum for a certain FD event. A power-law spectrum would be expected for rigidities ⩾1.68 GV (energies ⩾1 GeV). Furthermore, the spectrum for large FDs may deviate from the simple form of a power law. Adding to this, recently Munini et al. (2018), using PAMELA data covering a range of rigidities from 0.5 to 20 GV, employed (for the rigidity dependence of the amplitude) a power law and an exponential fit and concluded that the exponential fit is more suitable. However, in the current work we made the simplest and most common approximation for the spectrum, selecting a power law. A more detailed

[9] See explanation on the maximum of solar activity in the text.

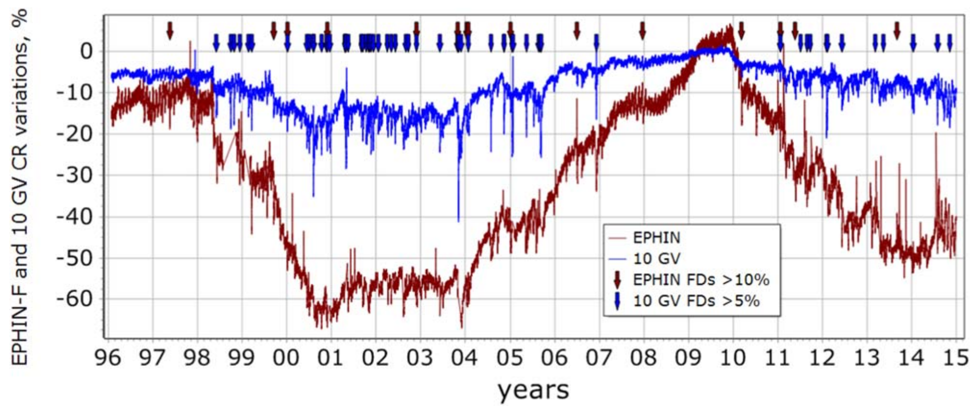

Figure 4. The long-time CR variations observed by the EPHIN F detector on board SOHO (brown line) and by NMs at Earth for a fixed rigidity of 10 GV (blue line). Arrows signify large FDs in terms of magnitude and follow the same color code per instrument. The base period used for the normalization is 2003 November.

investigation of the form of the spectra is beyond the scope of this study.

2.3. EPHIN and NM Data Combined

The long-term variations observed by EPHIN and by NMs at Earth (for a fixed rigidity of 10 GV) for the complete time span of our study (i.e., 1995–2015) are given in Figure 4. The EPHIN measurements are depicted with a brown line, and the NM observations with a blue line. As can be seen, the EPHIN measurements follow the dependence on solar cycle that is evident in the NM observations. Moreover, occasional enhancements associated with SEPs and decreases associated with FDs are evident. Thus, EPHIN is ideal for the purposes of this study, which aims at identifying FDs observed by EPHIN and NMs, comparing their magnitudes (as a percentage) and expressing this difference as a power law in rigidity. The arrows in the uppermost part of Figure 4 denote the largest FDs recorded at both SOHO and Earth, specifically those with amplitudes $A_E > 5\%$ for FDs observed by NMs at a fixed rigidity of 10 GV and $A_S > 10\%$ for SOHO/EPHIN FDs. One may note that large FDs recorded by NMs are much more frequent than satellite ones (i.e., if one compares the relative number of arrows). In addition, the lack of coincidence between a brown arrow (i.e., FD recorded by EPHIN) and a blue one (i.e., FD recorded at Earth) does not mean that there was no FD present at a fixed rigidity of 10 GV. The FD exists, but its magnitude falls slightly below the threshold of $A_E > 5\%$ and thus it is not counted. In contrast, when the blue arrow does not have a corresponding brown one, it is usually due to the fact that the EPHIN FD could not be selected—usually because of the masking due to SEPs (Dumbović et al. 2020).

3. Results

3.1. Identifying Forbush Decreases at EPHIN

For this study, we use EPHIN data between 1995 December and 2015 February. Within this time range, the FEID database contains a total of 2234 FD events, recorded at Earth. With the aim of selecting FDs that were observed both at EPHIN and on the ground by NMs we first selected those that, as a rule, were initiated with the arrival of an IP shock wave, marked by an SSC. We retrieved 483 such events from FEID, covering the time span of our analysis. However, when examining the SOHO/EPHIN data, often there were enhanced fluxes of SEPs present, in some cases accelerated by the ICME-driven shock. Although SEPs can also be modulated by the passage of ICMEs (e.g., Sanderson et al. 1990; Cane et al. 1993; Richardson & Cane 2011), they dominate over the GCRs (Dumbović et al. 2020) and have a different energy spectrum, and hence the GCR modulations cannot be examined using the EPHIN data for these FDs. Removing such events reduced the sample of FDs associated with an SSC to 252 events. To increase our sample size, we added FDs recorded at Earth by NMs with $A_E \geqslant 2\%$, at a fixed rigidity of 10 GV, that also coincided with a clear FD observed by EPHIN. Finally some events with $A_E < 2\%$ and with clear EPHIN FDs were also included. The final sample consists of 421 FDs observed at L1 by EPHIN on board SOHO and at Earth by NMs (the complete list is available in a machine-readable form in the online journal).

3.2. Catalog of FDs Recorded by EPHIN and Comparison with FDs Recorded by NMs

Figure 5 provides the magnitude of the FDs at Earth (A_E, %) for a fixed rigidity of 10 GV on the abscissa axis and the magnitude of the FDs at EPHIN on board the SOHO spacecraft (A_S, %) on the ordinate axis. Both A_E and A_S are determined using single data points derived from either GSM (i.e., A_E) or EPHIN (A_S) and correspond to the maximum of the CR variations during the event. For the identification of an FD, the starting point is the time when an SSC is marked. Then for the GSM output (i.e., NM recordings at Earth) we have applied an automated identification algorithm. The algorithm treats the SSC time as the starting point and further assumes that the time of maximum (t_{max}) is the actual start of the FD and coincides with the time of the SSC, while the time of minimum (t_{min}) is left open and is re-evaluated at every hour. Consequently, the maximum (Max) and the minimum (Min) of the hourly CR density variations are identified. The FD magnitude is defined as the difference in measurements $\delta = (\mathrm{Max}-\mathrm{Min})/\mathrm{Max}$ as a percentage. As a result the base period does not affect the amplitude determination. Additionally, all FDs identified in this manner were visually inspected and cross-checked with respect to their solar origin and interplanetary conditions. The amplitude was either confirmed or re-evaluated at this point, as well.

The accuracy in both NMs (i.e., GSM outputs) and EPHIN for the hourly CR variations is sufficient for the effective determination of FDs in both data sets. In particular, for the GSM output, the accuracy is 0.05%–0.06% (Belov et al. 2018) while for EPHIN it is 0.12%–0.2% (Kühl et al. 2015). Recently

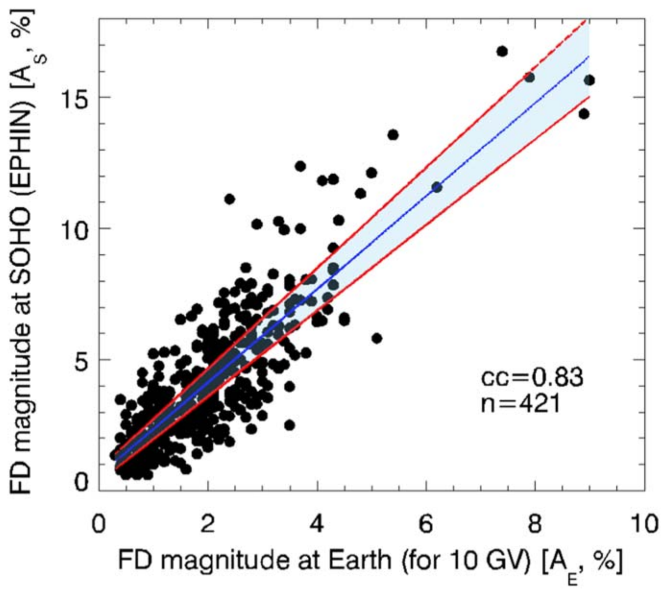

Figure 5. Relation between the magnitudes for FDs caused by the same interplanetary disturbances observed by the EPHIN F detector (A_S) and by NMs at Earth at 10 GV (A_E). Small circles represent individual episodes of FDs on SOHO and at Earth. The red lines depict the upper and lower limits of a 2σ error band, which is further color-coded in light blue. The least-squares linear fit is presented in dark blue, within the error band. *cc* denotes the correlation coefficient and *n* the number of pairs used.

automated methods for the identification of FDs have been proposed (e.g., Okike 2020; Light et al. 2020). In particular, Okike (2020) has investigated the use of an automated procedure to identify the magnitude of a FD versus the method using single data points that is traditionally applied in FD research—as in our case—and has highlighted the inherent trade-off between the usage of single data points and automated solutions. The former provides better resolution, while the latter has a higher statistical accuracy. However, the accuracy of the data sets employed in our study allowed for a detail identification of the FDs and their corresponding magnitudes.

Belov (2009) has reported FDs extending to ∼30% at 10 GV in NM observations, but these are evidently not included in Figure 5. This is because the largest FDs occur at times of high solar activity when SEPs are present and the FD cannot be observed by EPHIN. For example, within the period of our study (1995–2015) there were 12 FDs recorded at Earth (at a fixed rigidity of 10 GV) with a magnitude of $A_E > 10\%$, with one, in 2003 October, reaching almost 30%. All were recorded in periods of extreme SEP events. In Figure 5, all the NM FDs have amplitudes $A_E < 10\%$, and none of the FDs observed by EPHIN exceeds 17% (i.e., $A_S < 17\%$).

A fairly reasonable correlation ($cc = 0.83 \pm 0.03$) is evident and a linear linear relation (see Equation (2) below) between the magnitude of the FDs at SOHO/EPHIN (A_S) and the magnitude of the FDs at Earth (A_E) is obtained. As can be seen, the amplitude of the FDs at EPHIN is larger than the amplitude measured at Earth by NMs. The linear relation is given by

$$A_S = (0.58 \pm 0.13) + (1.77 \pm 0.06)A_E. \quad (2)$$

According to this dependence, A_S exceeds A_E by approximately a factor of 2. This is in qualitative agreement with the results obtained from Richardson & Cane (2011), who compared the amplitude of FDs recorded by the Goddard Medium Energy (GME) instrument on the IMP 8 spacecraft and the variations of

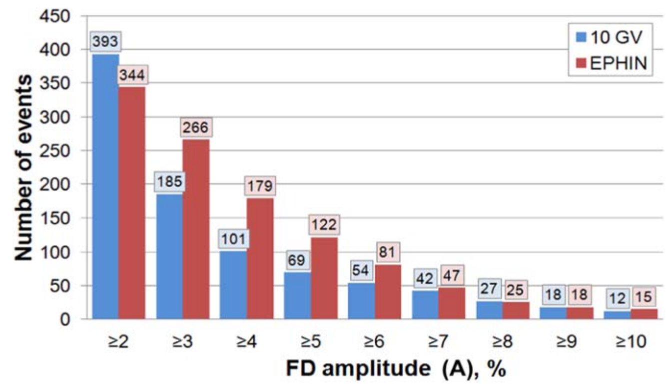

Figure 6. Distribution of the number of Forbush decreases with respect to their size (A) for GCR variations recorded at Earth, at a fixed rigidity of 10 GV (blue bars) and by EPHIN (brown bars).The *y*-axis provide the number of events. Numbers at the top of the bars indicate the actual number of FD events spotted at EPHIN and Earth, as a function of events in each amplitude bin indicated on the *x*-axis.

the Thule neutron monitor ($R_c = 0.30$ GV). Additionally, it may be noted that when A_E approaches zero, A_S tends to a small but nonzero value. This is due to the fact that small IP disturbances have almost no effect on particles at a fixed rigidity of 10 GV but may affect particles with lower rigidity (energy) recorded at EPHIN on board SOHO.

Figure 6 presents the number of FDs recorded by EPHIN, as well as all of those FDs recorded at Earth by NMs during the time span of the study, ordered with respect to their size (A); the integral bins range from $A \geqslant 2\%$ to $A \geqslant 10\%$ with an increment of 1%. Since the effective rigidity response of the EPHIN F detector is much lower than 10 GV (it varies from ∼1 to ∼1.5 GV, but the peak does not change significantly with respect to the solar conditions, see Figure 3), there are more FDs of a given size observed by EPHIN in Figure 6, at least up to $A \geqslant 7\%$. Beyond this size, the numbers of events are approximately equal. This is due to the fact that the largest FDs are created by powerful, broad, and fast CMEs, which, as already discussed, are often effective accelerators of SEPs (see, e.g., Cane et al. 2010; Papaioannou et al. 2016). Therefore, almost inevitably, all FDs of significant magnitude ($A_S > 17\%$ in SOHO/EPHIN data; see the upper limit on the *y*-axis of Figure 5) coincide in time with large SEPs and hence EPHIN was unable to detect the FD. Additionally, SEPs can affect the identification of small FDs, but to a lesser extent. This indicates why, for the group of FDs with the smallest amplitude in our analysis, the absolute difference in FDs observed at Earth and at EPHIN was the smallest. Finally, one should note that the smallest A_S in our selection for this sample is 0.6% and the smallest A_E is 0.3%, both significantly larger than the statistical accuracy of the respective observations. Note that the statistical accuracy for the GSM outputs is 0.05%–0.06% (Belov et al. 2018) while for EPHIN it is 0.12%–0.2% (Kühl et al. 2015).

3.3. Rigidity Dependence of FDs: Similarities and Exceptions

3.3.1. Example events

Figure 7 compares energetic particle and solar wind observations in the vicinity of a shock and an ICME/MC, in order to demonstrate how GCRs respond to the passage of these structures, resulting in the FD, and also to illustrate how solar wind observations provide context to the GCR observations. The arrival

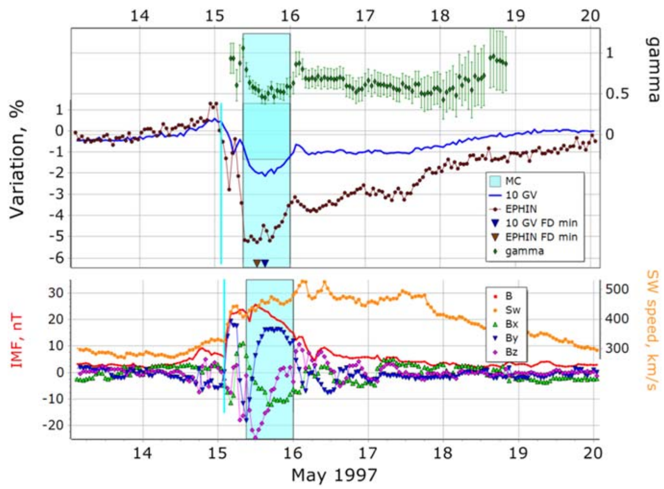

Figure 7. GCR density variations as recorded at Earth by the worldwide neutron monitor network, at a fixed rigidity of 10 GV (blue line), together with GCR variations recorded at EPHIN, on board SOHO (brown points connected with a continuous line) for the same time span from 1997 May 13–20. The blue vertical line corresponds to the arrival of the shock, the light blue rectangle presents the MC that was identified in this period, while the triangles depict the moment of the FD minimum at both NM and EPHIN measurements.

of the shock at Earth (the SSC) is denoted with a light blue vertical line in both panels. A strong enhancement in the total magnetic field B (bottom panel; red line) is observed, peaking at $B_{\max} = 25.3$ nT around a day after the shock. Following the shock, a sheath region that lasts ∼6 hr is observed. Then, an MC arrives (see Webb et al. 2000; Owens 2006), marked by the transparent light blue rectangle in both panels.

Both EPHIN (top panel; brown line) and the NM network (top panel; blue line) show a clear GCR depression. This depression commences at the shock and extends into the sheath region constituting the "first step" of the FD. A second decrease (i.e., the "second step") occurs upon entry into the ICME/MC, reaches maximum depression almost at the middle of the MC (denoted by arrows in the top panel of Figure 7, colored blue for Earth and brown for EPHIN). Then both densities start to recover. The evolution of γ_F obtained from the EPHIN and NM measurements is further presented in the top panel for each hour of measurements, as green diamonds (including errors, e.g., σ_γ).

As noted in Section 1, two different structures contribute to FDs, driven by ICMEs: the sheath with the shock at the leading edge, and the ICME. As a result, the first step of the FD begins at the shock and continues into the turbulent sheath region, while a second step commences at the tangential discontinuity at the ICME's leading edge (Cane 2000; Belov 2009; Jordan et al. 2011). As already mentioned, our selected event, which covers the time span from 1997 May 13–20, is a textbook *two-step* FD, driven by an ICME with an upstream sheath, evident in both measurement sets. The corresponding maximum magnetic field strength was reached in the center of the MC, while the solar wind speed was still elevated during the MC and reached its maximum ($V_{\rm SW} = 527\ {\rm km\ s^{-1}}$) after its passage. Inspection of Figure 7 indicates that there is a very good agreement between the time profiles of the FD recorded at SOHO by EPHIN and at Earth by NMs, with the time of minimum observed by NMs delayed by only ∼1 hour from the minimum observed by EPHIN. However, apart from the general form of the time profile, there are also some similarities in the finer structures in each time profile. The rigidity dependence of the corresponding magnitude of the FD, assuming an inverse power-law dependence, yields $\gamma_F = 0.50 \pm 0.06$ (see the complete list in a machine-readable form in the online journal).

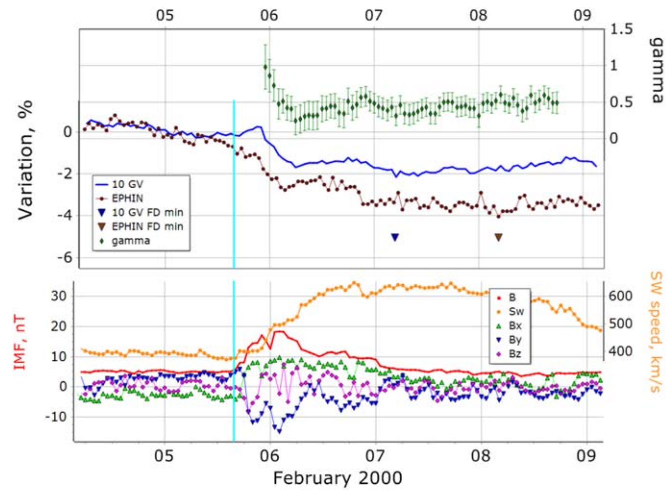

Figure 8. Similar to Figure 7 for a recurrent short-term GCR density variation in the time period from 2000 February 5–9.

Figure 8 presents a similar comparative plot to Figure 7 but for the case of a recurrent short-term GCR modulation, driven by a high-speed stream that extended from 2000 February 5–9. The forward shock of the CIR at the leading edge of the stream is indicated with a light blue vertical line. The smooth rising then declining time profile of the solar wind velocity is evident in the bottom panel (orange line). The solar wind speed had a maximum of $V_{\rm SW} = 649\ {\rm km\ s^{-1}}$, while the maximum of the magnetic field strength (bottom panel; red line) is $B_{\max} =$ 18.3 nT. The time profiles observed by NMs (top panel; blue line) and EPHIN (top panel; brown line) both show the GCR density decreasing in close anticorrelation to the solar wind speed (Melkumyan et al. 2019), which is consistent with the fast solar wind sweeping CRs away from the Sun (see Richardson (2018) and references therein). The GCR minimum is observed by NMs more than a day after the start of the FD, and after about two days by EPHIN (as denoted by the triangles in the top panel of Figure 8).

3.3.2. *Differences between Events*

The correlation between the FD magnitudes observed by NMs and EPHIN obtained in Figure 5 suggests that there is a typical, representative rigidity dependence for FD magnitudes. However, there are events that significantly differ from this average (mean) behavior, such as those shown in Figure 9. The FD magnitudes observed by NMs and EPHIN differ by a factor of ∼4 in the 2010 April 4–10 event (top panel) but are similar in the 2001 May 26–June 1 event (bottom panel). Investigating this further, we find that both cases are driven by ICMEs that had MCs. However, in the first case (i.e., 2010 April 4–10) the sheath region following the shock (depicted as a vertical light blue line) lasts only ∼4 hr prior to the MC arrival (presented as a light blue rectangle). The minima of the FD for both EPHIN and Earth occurred within the MC as indicated by the corresponding triangles, but the minimum observed by EPHIN was around 6 hr before that observed by NMs. The fast MC ($V_{\rm SW} = 814\ {\rm km\ s^{-1}}$) with an enhanced magnetic field ($B_{\max} = 18.8$ nT) might be expected to efficiently

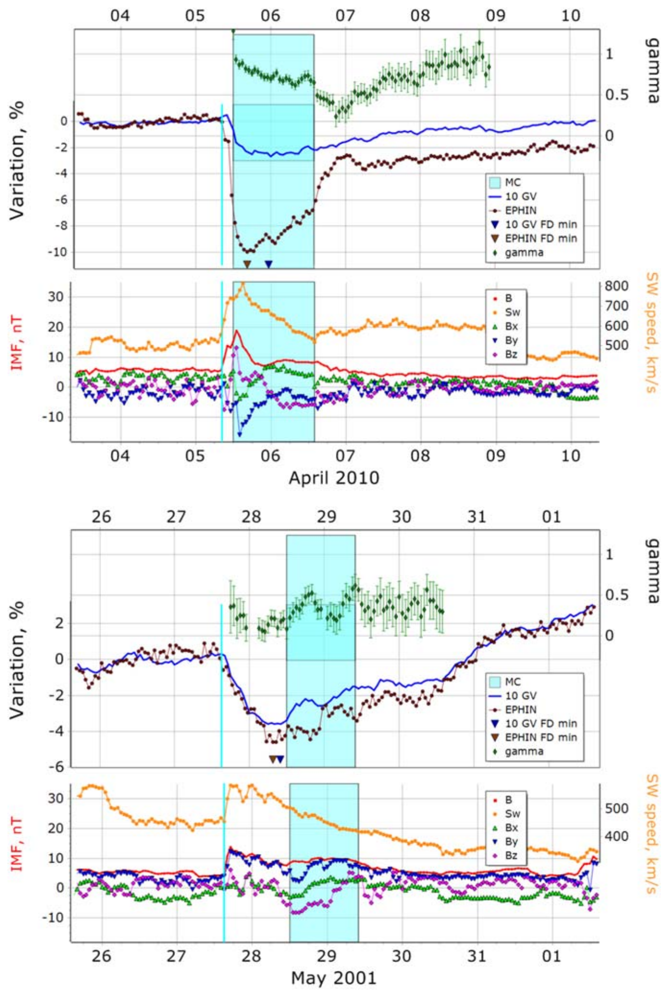

Figure 9. Similar to Figure 7 for the time periods 2010 April 4–10 (top panel) and 2001 May 26–June 1 (bottom panel).

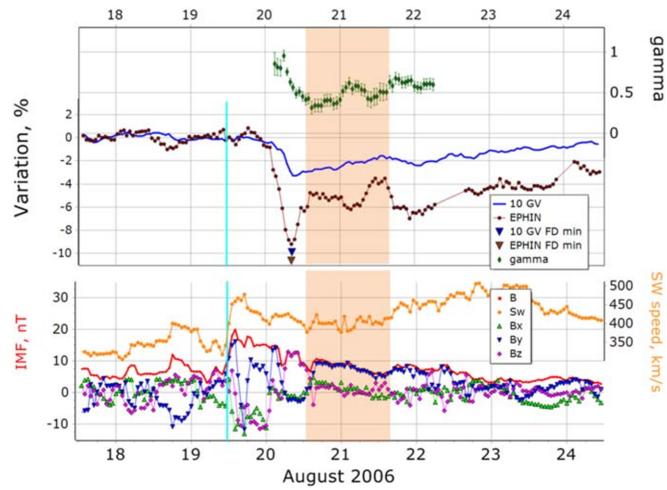

Figure 10. Similar to Figure 7 for the time period 2006 August 18–24.

modulate GCRs, and this is demonstrated by the resulting magnitude of the FD, which is $A_S = 10.16\%$ for SOHO/EPHIN and $A_E = 2.9\%$ for NMs, leading to a rigidity dependence given by $\gamma_F = 0.71 \pm 0.04$. On the other hand, in the second case (i.e., 2001 May 26–June 1) the driving ICME led to a shock (depicted as a vertical light blue line), followed by a sheath region that lasts almost 19 hr, prior to the arrival of the MC (which is marked as a light blue rectangle). It can be seen that the minima of the FD at both L1 and Earth occur in the sheath just ahead of the MC and close together in time. This event had $A_S = 5.44\%$, $A_E = 3.5\%$, and $\gamma_F = 0.28 \pm 0.08$. Both the maximum of the solar wind speed ($V_{SW} = 587\,\mathrm{km\,s^{-1}}$) and the maximum of the magnetic field strength ($B_{max} = 13.9\,\mathrm{nT}$) occur in the turbulent sheath region soon after the arrival of the shock. Comparing these two events, it seems that both the shock–sheath part and the ICME/MC part can have an independent role in the development of FDs but both are necessary for the establishment of the deepest FDs (in terms of magnitude); this is especially highlighted in this work in the SOHO/EPHIN measurements—in line with the results of Richardson & Cane (2011) and Papaioannou et al. (2020).

3.3.3. Differences during the Same Event

The rigidity (energy) dependence of the CR variations can also occur during an individual event. For example, significant differences in the time profiles observed by NMs and EPHIN can be identified in Figure 10, which shows observations from 2006 August 18–24. The variations of GCRs recorded by EPHIN demonstrate a rather complicated behavior during the recovery phase of the FD, in particular from 2006 August 20–21. This particular FD is driven by an ICME, whose leading disturbance (i.e., shock) arrived at Earth on 2006 August 19 (SSC at 11:31 UT; denoted by a light blue vertical line on the plot), followed by the ejecta (which was not characterized as an MC), almost 14 hr later (indicated by the orange rectangle). The start of the FD is observed several hours after the arrival of the shock. The minimum of the FD occurs prior to the crossing of the ejecta for both EPHIN and Earth. In addition, a stream from a coronal hole facing the Earth on 2006 August 18 affected near-Earth space from 2006 August 21–23, gradually pushing the solar wind speed to $\sim 500\,\mathrm{km\,s^{-1}}$ and interrupting the recovery of the FD. Moreover, a CR decrease of smaller magnitude is evident in SOHO/EPHIN measurements (brown line) on 2001 August 18, preceding the main FD. However, most of these features are not clearly observed in NM data (blue line; at a fixed rigidity of 10 GV), showing that the interplanetary propagating structures modulated GCRs of lower rigidity (energy) more effectively than those of high rigidity (energy).

Since such structures can modulate CRs of lower rigidity more effectively, two-step structures might be expected to be observed more frequently in observations at lower rigidity made by spacecraft. This is illustrated in Figure 11, which depicts the FD on 2002 May 18–21 as recorded by EPHIN and at Earth. Plasma data reveal the arrival of a shock (denoted with the light blue vertical line) and an MC (denoted by the light blue rectangle). The minimum of the FD for both observing sites (e.g., L1 and Earth) occurs within the MC. However, NM measurements (blue line) are not capable of distinguishing between the two steps of the FD, while EPHIN measurements (brown line) are. From inspection of all 421 FD events identified in the EPHIN data we have identified the characteristic two-step FDs in 116 cases (116/421, ∼27% of the total sample), in contrast to NM recordings where such events were fairly rare (i.e., 58/421 FDs, ∼14% of the total sample) (see also Papaioannou et al. 2020). It may be concluded that lower rigidities (energies) are better suited for studying small-scale features in FDs and their association with

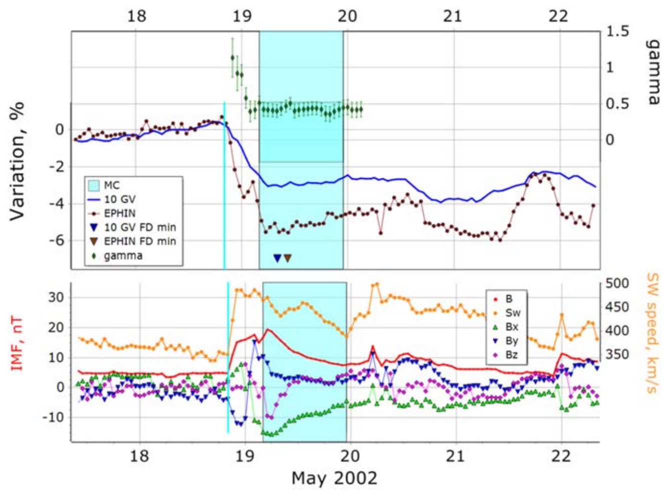

Figure 11. Similar to Figure 7 for the time period 2002 May 17–22.

local solar wind structures such as ICMEs. In turn, this points to the fact that the identification of FDs via particle detectors on board spacecraft (if no interference from SEP fluxes is present) can be used for the efficient tracking of solar wind transients, in line with previous works (e.g., Cane et al. 1994, 1997, 1998, 2000; Richardson 1997).

3.4. Characteristics of the Rigidity Spectrum for FDs Recorded by EPHIN on board SOHO

Comparison of the FD catalogs based on SOHO/EPHIN and NM data, respectively, provides a direct determination of the rigidity spectrum under the assumption of a simple rigidity dependence, e.g., an inverse power law (Dumbović et al. 2020) that is characterized by the determination of a single parameter: the exponent γ. Such an exponent has been recently identified for the 10 GV particles by GSM (Belov et al. 2018) and is included in the description of the FD events in FEID (Klyueva et al. 2017). However, such an exponent can only be quite accurately determined for sufficiently large FDs. With FD events identified concurrently at two observational points with different rigidities (energies) for a continuous long time span of ~20 yr, a more accurate determination of the slope of the FD spectrum can be searched for.

We obtained estimates of the spectral index γ_F of the rigidity spectrum of the CR variation at the FD minima for all 421 events. However, the accuracy of these estimates is different: the spectral index is determined much more accurately for large FDs (in terms of magnitude) than for smaller ones. The standard statistical error of γ_F varies from 0.03 to 0.60. However, large errors are encountered infrequently and $\sigma_\gamma > 0.15$ is obtained for ~1/3 of the events (~33%). Figure 12 shows that the distribution of γ_F is rather narrow; the half-width of the corresponding Gaussian function is ≈0.2. About 2/3 of all events (~67%) have γ_F within the range 0.3–0.7. The mean value of γ_F, together with its standard error of the mean, is $\langle\gamma_F\rangle = 0.46 \pm 0.02$ for all 421 events. For the same events, the average value of the analogous index determined only from the data of NMs is 0.57 ± 0.02. This difference in the obtained $\langle\gamma_F\rangle$ is probably related to the difference in the rigidity dependences; i.e., for NMs, this was determined for 10 GV, while in this work, it is determined for the range ~1.0–10 GV.

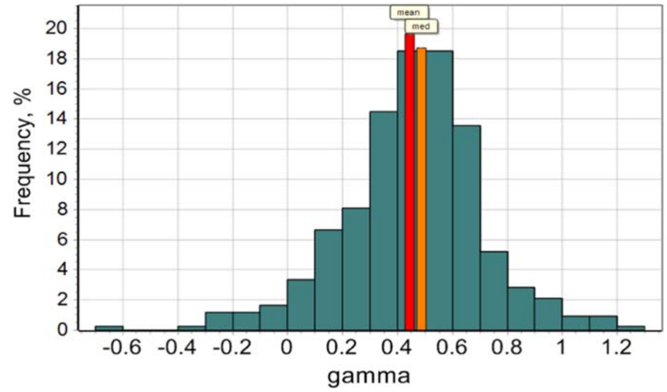

Figure 12. The distribution of γ_F obtained for the FDs recorded by EPHIN on board SOHO. The red bar denotes the mean value and the orange bar denotes the median of the distribution.

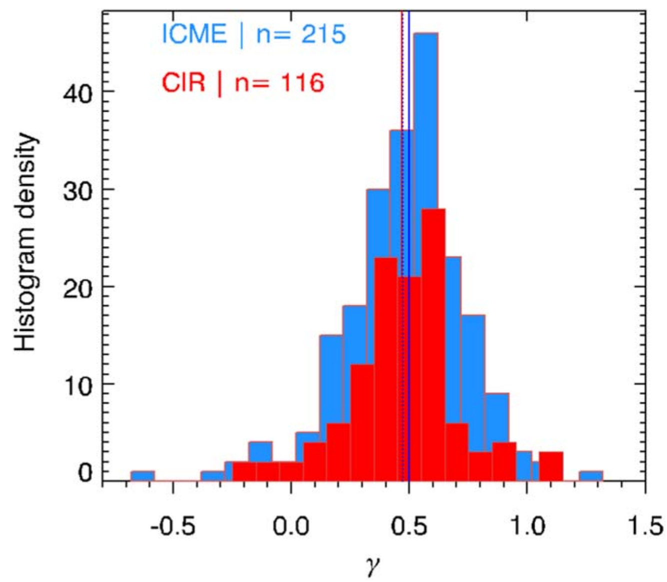

Figure 13. The distribution of the γ_F for FDs associated with ICMEs (blue) and CIRs (red). The number of cases per category (n) is included on the plot. The vertical solid lines provide the median of the distributions, and the dashed ones the mean.

FDs with a soft spectrum (i.e., a large spectral index) are almost absent (Figure 12). $\gamma_F > 1$ occurs only nine times, and the largest value is $\gamma_F = 1.26 \pm 0.18$. Abnormally hard spectra (small indices) are more more frequent—19 cases had negative γ_F, which corresponds to an increase in the size of the FD at higher rigidities rather than a decrease, as usually expected. However, the absolute value of the majority of these anomalies (i.e., $|\gamma_F| < 0.2$) is rather small, and the statistical error for them is generally large ($\sigma > 0.2$), so it is very likely that almost all of these anomalies are the result of random fluctuations. Nevertheless, the analysis of all FD events in this work leads to the conclusion that abnormally hard FD spectra can occur, and possibly even spectra with inverse rigidity dependence.

From the total sample of 421 FD events, we selected 215 that could be reliably associated with an ICME and 116 that were linked to a CIR (or to a possible CIR labeled as CIR? in the complete list presented in machine-readable form in the online journal). Figure 13 shows the distributions of γ for these two sets of events, where the dashed or solid vertical lines indicate the

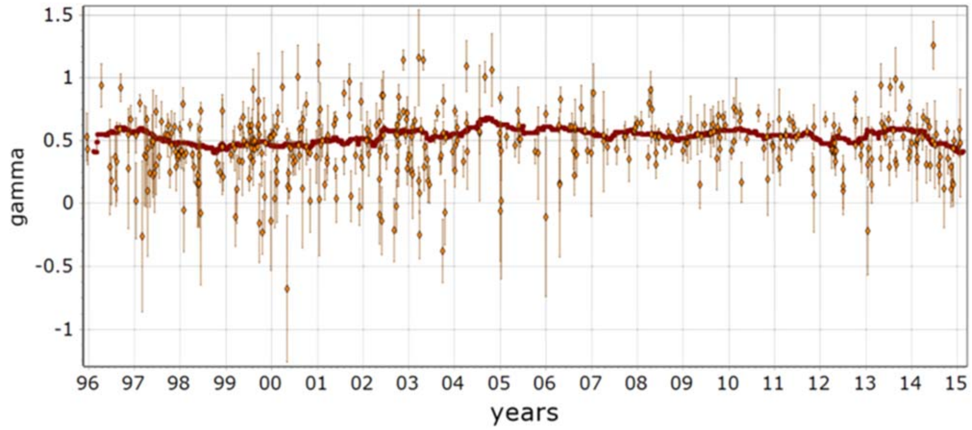

Figure 14. The long-term behavior of the rigidity spectrum γ_F of FDs recorded on board SOHO by EPHIN from 1995 to 2015. A yearly running average of the index is displayed as a continuous line.

mean or median values, respectively. ICME events are presented in blue and CIR events in red. The distributions show a remarkable similarity, which is further highlighted by $\langle\gamma_F\rangle$, which is 0.47 ± 0.02 for FDs associated with both ICMEs and CIRs (shown as overlapping dashed lines in Figure 13). At the same time, median values (presented as solid lines) differ slightly, with the FDs associated with ICMEs reaching $\gamma_F = 0.50$ and those associated with CIRs $\gamma_F = 0.47$. Klyueva et al. (2017) showed that for $n = 19$ FDs associated with CIRs from coronal holes, $\langle\gamma_F\rangle = 0.504 \pm 0.026$, while for $n = 69$ FDs associated with a solar flare, which in turn pointed to an ICME (including ICMEs that had an MC), $\langle\gamma_F\rangle = 0.637 \pm 0.016$ (see their Table 3). In order to investigate this further, these authors categorized their samples based on the identification of an SSC. They showed that for $n = 133$ SSCs, $\langle\gamma_F\rangle = 0.660 \pm 0.013$, while for 85 cases when no SSC was observed, $\langle\gamma_F\rangle = 0.487 \pm 0.023$ (see their Table 4). The typical spectrum obtained for recurrent FDs seems to be harder than the one obtained for sporadic sources (see, e.g., Klyueva et al. 2017). Our results (Figure 13) do not show this difference in the spectra clearly, though there is a similar trend in the median values of $\langle\gamma_F\rangle$.

Figure 14 shows γ_F for all 421 FD events with respect to the time span of the study. Points corresponds to the γ_F values with with the 1σ errors indicated. The heavy brown line corresponds to a yearly average of the γ_F values. Evidently, over the complete study period, the yearly averages of γ_F show small variations that do not follow the solar cycle. The spread of γ_F values is larger during the period of increased solar activity (1999–2003) in solar cycle 23 than in the relatively quiet period of 2007–2011. Most of the FDs at solar minimum are associated with CIRs (similar to the event in Figure 8), which is suggestive of less event-to-event variation in the rigidity dependence of FDs associated with CIRs. In addition, the spread of γ_F values is larger from 1995 until 2006 (i.e., during solar cycle 23) than the variations in γ_F observed in solar cycle 24 (2012–2014) (see Figure 14). Therefore, γ varies more in solar cycle 23 than in cycle 24. To quantify the spread in γ, Figure 15 shows the distribution of σ_F for three time periods, colored blue for 1999–2003, red for 2007–2011, and orange for 2012–2014. The largest range of σ_F values (i.e., 0.55) is obtained in the period of increased solar activity (1999–2003). The lowest range (i.e., 0.37) is retrieved in the relatively quiet period of solar cycle 23 from 2007 to 2011, while an approximately similar range (i.e., 0.39) is obtained in solar

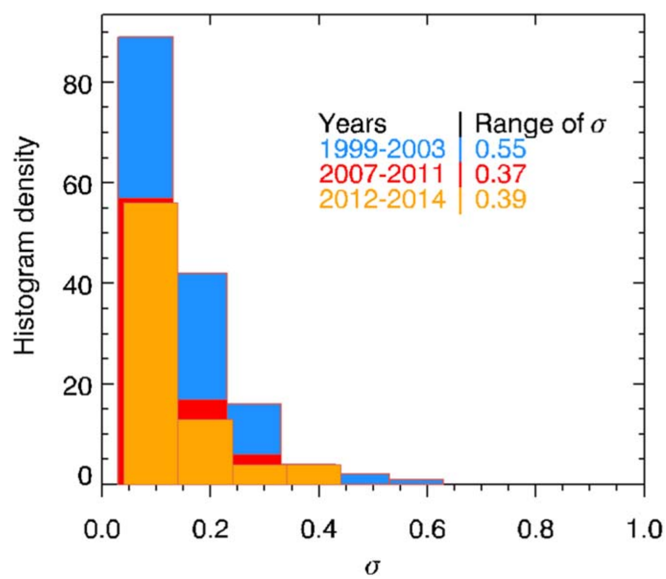

Figure 15. The distribution of σ_γ for three time periods: 1999–2003 (blue), 2007–2011 (red), and 2012–2014 (orange). The relative range of σ values for each time period is indicated on the plot.

cycle 24 (2012–2014). Thus, when disturbed conditions are in effect (i.e., at solar maximum), with multiple events occurring and propagating in IP space, there is a large spread of γ values. In contrast, at solar minimum and when mild conditions prevail in IP space (i.e., solar cycle 24 with reduced field strength and speed of MCs arriving at Earth) (Gopalswamy et al. 2015), γ values have a smaller spread.

3.5. The Behavior of the Rigidity Spectrum of CR Variations inside Interplanetary Disturbances

Significantly large changes of the rigidity spectrum γ_F can be seen within a short time during a single FD event. Several illustrative examples follow.

The onset of the FD on 1997 April 10 (Figure 16) coincides with the arrival of a shock wave (SSC at 12:58 UT; denoted by a light blue vertical line on the plot). Furthermore, an MC is present (denoted by the light blue rectangle) from 06:00 to 19:00 UT on the following day (1997 April 11). The FD has a classic two-step structure in the SOHO/EPHIN measurements (brown

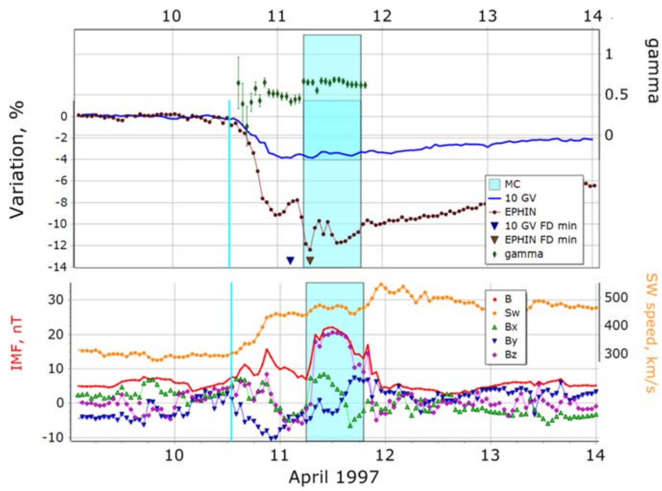

Figure 16. Similar to Figure 7 for the FD that was recorded from 1997 April 9–13.

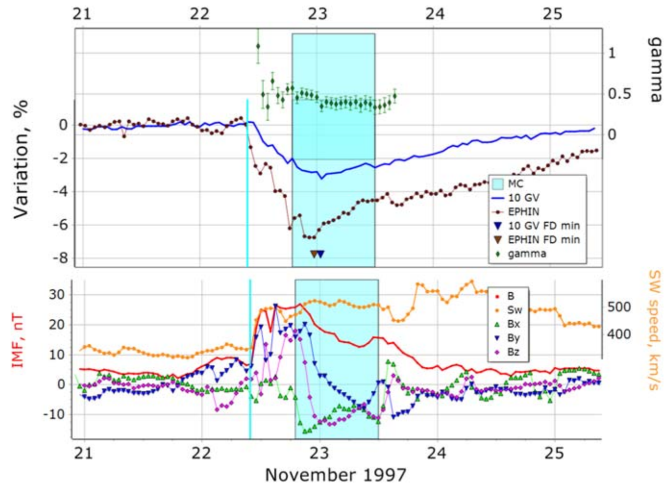

Figure 17. Similar to Figure 7 for the time period 1997 November 21–25.

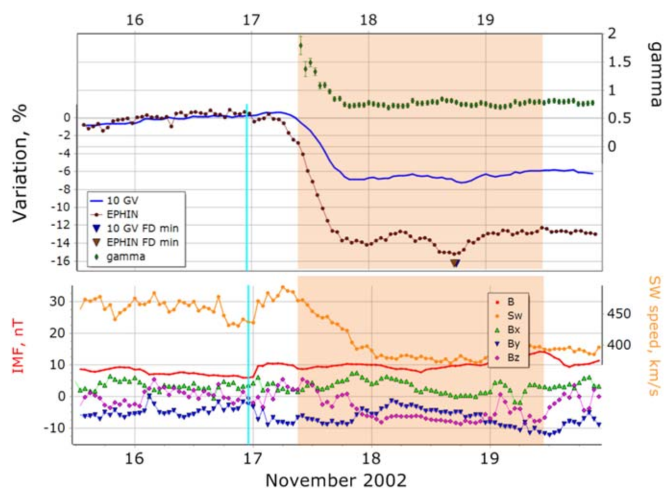

Figure 18. Similar to Figure 7 for the time period 2002 November 15–19.

line), although the second step is not noticeable in the NM observations at a fixed rigidity of 10 GV (blue line). The selected time period is very complex (see Berdichevsky et al. 1998) and this further pertains to the short-term modulation of GCRs. At the beginning of the intensity decrease, γ_F is small but the errors are relatively large. The spectrum of the first step of the FD stabilizes 5–6 hr after the onset of the event, and the average γ_F for the period from 19:00 UT on April 10 to 05:00 UT on April 11 is 0.47 ± 0.01. At about 06:00 UT on 1997 April 11 (i.e., the start of the MC crossing), a sharp softening of the spectrum occurs, γ_F becomes >0.6, and its average value for the period from 06:00 to 18:00 UT on 1997 April 11 (during the passage of the MC) is 0.65 ± 0.01. The abrupt change in the spectrum coincides in time with the entry of the Earth into the MC and the beginning of the second step of the FD (Richardson & Cane 2010). This MC is observed for $\sim$13 hr, but the IMF in it was quite strong ($B_{\max}$ reaches 22.5 nT based on hourly data).

The FD on 2001 May 27 discussed above and illustrated in the bottom panel of Figure 9 also shows variations in γ_F during the event. In the declining phase of the FD the variation of the spectral index indicates a gradual hardening, which leads to abnormally hard values near the minimum of the CR density (i.e., FD minimum). The trend changes and the index starts to increase right before the FD minimum. It then continues to grow as the Earth enters the MC (time of MC passage from 12:00 UT on 2001 May 28 to 10:00 UT on 2001 May 29) and changes regularly within it. The well-defined region of the lowest CR density (from the first hours of May 28 to the end of the day) coincides with the sheath region between the shock and the MC crossing (marked by the light blue rectangle). Nevertheless, this minimum coincides with the lowest plasma temperature (not shown), which extends to the end of May 29 (hence extending further from the upper boundary of the MC). During the recovery phase, a gradual softening of the spectrum is observed. It is noteworthy that, in this case, changes in γ_F can be seen during an FD that was not very large in terms of magnitude (i.e., $A_S \leqslant 5\%$). Figure 17 shows the FD event on 1997 November 21–25. This event is associated with a shock marked as an SSC on November 22 at 09:49 UT. The sheath region lasts for $\sim$9 hr and is followed by an MC lasting for 17 hr. The minimum of the FD occurs for both EPHIN and Earth within the MC, as denoted by the respective triangles. The softening of the variation of the spectrum in the recovery phase is evident in this case as well.

The FD on 2006 August 20–22 discussed above (Figure 10) is associated with an ICME that was not characterized as an MC and the FD minimum occurs concurrently for both EPHIN and NMs. There is a significant change of the spectrum in the declining phase of the FD, with γ_F shifting from 0.95 to 0.32 during that time. Once within the ICME, the FD at Earth (blue line) seems to enter a gradual recovery phase, whereas the response of EPHIN shows specific features (i.e., a plateau that lasted for almost 9 hr, followed by a small increase, and then entry into the recovery phase as well). During this time, changes in γ_F are also observed. However, as a whole, such abrupt changes in the observed behavior of γ_F do not constitute the usual case for most of the FD events, based on the sample used in this study.

Finally, in Figure 18 the FD event on 2002 November 15–19 is presented. In this period an ICME commencing on 2002 November 17 is identified in the plasma data. There is a shock that coincides with the start of the FD at both EPHIN and Earth and an ICME that lasts from 2000 November 17 at 10:00 UT to 2000 November 19 at 12:00 UT (indicated by the orange rectangle). The minima of the FD in the EPHIN and NM data occur almost simultaneously within the ICME. In this case, abrupt changes in γ_F are only present in the decay FD phase, whereas after this part γ_F is fairly stable up until the end of the event with only a few slight variations in the obtained spectrum.

4. Mechanisms for FDs

FDs are caused by magnetic field variations associated with propagating solar wind transients (Cane 2000; Belov 2009). Parker (1965) introduced the transport equation of cosmic rays in the heliosphere, which includes contributions from four basic physical effects: (a) diffusion, (b) drift, (c) convection, and (d) energy change (Jokipii 1971). In the propagating diffusive barrier model (e.g., Wibberenz et al. 1998), an FD results from the smaller diffusive mean free path for GCRs in the turbulent magnetic field in the sheath region of an ICME between the shock and the ejecta. In this case, the rigidity (energy) dependence of the magnitude of the FD reflects the rigidity dependence of the diffusion coefficient $K = \lambda v/3$, where λ is the mean free path for the scattering and v is the particle's speed (Lockwood et al. 1991). The speed v of particles with a rigidity (energy) R (E) $>$ 2 GV (1.23 GeV) is practically constant, thus the magnitude of the FD should depend upon λ alone (for particles above this characteristic rigidity; Lockwood et al. 1991). As a result, the FD magnitude should scale as R^{-1}. If this is further extrapolated to lower rigidities ($R \leqslant 2$ GV) this would lead to a very steep rigidity dependence. However, the obtained γ from this current study is smaller than 1.00 (i.e., $\langle\gamma_F\rangle = 0.46 \pm 0.02$), indicating that the spectrum is flatter and is in fairly good agreement with recent independent studies (e.g., Klyueva et al. 2017). If one assumes that the FD is due only to diffusion, our results suggest that the diffusion coefficient (i.e., the mean free path) does not simply scale with R for lower-energy particles. Consequently this means that low-energy particles are less efficiently scattered. Such a result is in agreement with, for instance, the empirical form of the diffusion coefficient given in Potgieter (2013) and the fact that EPHIN covers the lower-rigidity region since it detects lower-energy particles than NMs.

Kadokura & Nishida (1986), building upon the work of Nishida (1983), modeled a two-dimensional FD in the presence and absence of particle drifts. Considering protons of rigidity (energy) 2 GV (1.51 GeV) and 6 GV (5.31 GeV), they found that the steepest inverse power-law event spectrum, having an exponent of 0.88, occurred in the absence of drift (Duldig & Humble 1992). They also showed than in the no-drift scenario there is a clear tendency of flattening the rigidity dependence of the FD below a rigidity (energy) of $\sim$1.5 GV (800 MeV), demonstrating that the enhancement of the magnetic field is essential to the decrease of GCRs (Lockwood et al. 1991). Recently, Munini et al. (2018) utilized PAMELA data and presented the rigidity dependence of the amplitude of the FD in 2006 December 13–22, from 0.4 to 20 GV. Using a power law in rigidity, they obtained a spectrum (γ) of 0.45 ± 0.02, which is consistent with our findings.

The expansion of the ICME introduces further modulation effects in GCRs, and leads the adiabatic cooling of the particles (see Lockwood 1971 and reference therein). Moreover, Sanderson et al. (1990) has demonstrated that ICMEs that are characterized as MCs have a prominent role in the development of FDs, with Cane (1993) further showing that MCs contribute to the modulation of GCRs. As a result, the energy loss of the particles via adiabatic cooling should lead to additional reduction of GCRs and thus to larger FD amplitudes (at least locally in the ICME ejecta) (Papaioannou et al. 2010; Richardson & Cane 2011; Belov et al. 2015; Dumbović et al. 2018). Additionally, FDs with a larger amplitude associated with ICMEs more often have their minimum within the ICME/MC (Papaioannou et al. 2020). Moreover, GCR depressions related to ICMEs arise from the partially restricted access of the CR particles to the closed magnetic structure of the ICME/ejecta (Cane et al. 1995). In this case, CRs can penetrate into the ICME/ejecta primarily through cross-field diffusion (Munakata et al. 2006) and/or drift. Such a process is more efficient for low-energy particles, since they have greater difficulty in entering closed magnetic field structures along the average field direction from larger radial distances. Thus the effect would be more prominent for FDs observed by EPHIN than for those detected by NMs—as we have seen in a number of events in the current work.

5. Summary and Conclusions

The first extended comparative analysis of the rigidity response of GCRs to solar wind structures during FDs, calculated using observations from the worldwide NM network for a fixed rigidity of 10 GV and the measurements of EPHIN on board SOHO at L1, was performed in this study.

Based on data from EPHIN (F detector) on board SOHO spanning from 1995 December to 2015 February, 421 Forbush decreases were selected and a catalog of FDs observed by EPHIN and NMs on Earth was compiled. This is presented in full in a machine-readable form in the online journal. The FDs in the catalog mainly correspond to FDs recorded by NMs (at a fixed rigidity of 10 GV) with an amplitude $A_E > 2\%$ and with events initiated by the arrival of an interplanetary shock wave that led to an SSC. However, for around half of the NM FDs with amplitudes $A_E > 2\%$, and all those with amplitudes $A_E > 9\%$, SEPs were present in the SOHO/EPHIN data and hence these FDs were not included in the catalog of FDs compiled and used in this study. It was shown that the FDs observed at EPHIN have larger sizes (A_S) by a factor $\sim$2 than FDs recorded by NMs at Earth (A_E).

Comparison of the sizes of FDs recorded by EPHIN and by NMs makes it possible to estimate the spectral index (γ_F) of the spectrum assumed to be an inverse power law in rigidity, for all 421 selected SOHO/EPHIN FDs. As a rule, the γ_F index is determined with very good accuracy ($\sigma_F < 0.15$).

1. The average value $\langle\gamma_F\rangle = 0.46 \pm 0.02$ and the spectrum of FDs (for a range of rigidity from $\sim$1 to 10 GV) is somewhat harder than the spectrum of FDs observed by ground-based NMs alone (Klyueva et al. 2017).
2. As a general trend ($\sim$96%, 402/421 FD events) the amplitude of the FDs was found to decrease as the rigidity increased. However, in $\sim$4% (19/421) of the identified FDs the opposite was found, although with considerable statistical errors ($\sigma > 0.2$).
3. γ_F seems not to depend on solar cycle and shows small variations, with a larger spread during periods of more intense solar activity (1999–2003) than during quieter periods (2007–2011).
4. About 2/3 ($\sim$66%) of all FDs have γ_F in the range between 0.3 and 0.7. The remaining 1/3 of the events ($\sim$33%) have either (very) soft or hard FD spectra, with the latter being more common than the former. In

particular, ∼12% (52/421) of the FD events have $\gamma_F > 0.7$ and ∼22% (92/421) have $\gamma_F < 0.3$.

A preliminary comparison of the rigidity dependence between FDs driven by ICMEs and CIRs was performed and showed that:

1. the mean obtained spectral index is strikingly similar (i.e., $\gamma_F = 0.47 \pm 0.02$) in both subsamples,
2. median values of γ_F differ slightly, with FDs associated with CIRs showing a tendency to have a harder spectral index than the one obtained for sporadic ones.

However, such a comparison deserves a more thorough investigation and constitutes a natural next step, which is beyond the scope of this work.

Significant changes in the rigidity spectrum of CR variations occur within almost every FD. In particular:

1. during the FD decay phase the spectrum becomes gradually harder, while during the FD recovery phase it gradually softens,
2. when entering an MC, abrupt changes in the slope of the spectrum are observed.

Low rigidities (energies) seem to be better suited for the detailed study of the fine structure of interplanetary disturbances (primarily ICMEs), which lead to FDs, with *two-step* FDs being clearly recorded by EPHIN almost twice as often as FDs recorded by NMs at Earth. Finally, this work further verifies the usage of particle detectors on board spacecraft for the efficient tracking of solar wind transients.

SOHO is a project of international cooperation between ESA and NASA. We acknowledge the NMDB database (www.nmdb.eu), founded under the European Union's FP7 program (contract No. 213007) for providing the data. The "X-ray Flare" data set was prepared by and made available through the NOAA National Geophysical Data Center (NGDC). We acknowledge the use of the near-Earth interplanetary coronal mass ejection list compiled by I.G. Richardson and H.V. Cane (http://www.srl.caltech.edu/ACE/ASC/DATA/level3/icmetable2.htm). The SOHO/EPHIN project is supported under grant 50 OC 1702 by the German Bundesministerium für Wirtschaft through the Deutsches Zentrum für Luft- und Raumfahrt (DLR). Part of the research leading to these results was supported from the TRACER project (http://members.noa.gr/atpapaio/tracer/) funded by the National Observatory of Athens (NOA) (Project ID: 5063). M.A., A.B., and A.A. (IZMIRAN) are supported by the Russian Science Foundation under grant 20-72-10023. A.P., A.B., B.H., P.K., K.H., and E.E. acknowledge the discussions from the HEROIC team at the International Space Science Institute (https://www.issibern.ch/teams/heroic/). A.P. and I.G.R. acknowledge support from NASA/LWS project NNH19ZDA001N-LWS. M.D. acknowledges support by the Croatian Science Foundation under the project 7549 (MSOC) and EU H2020 grant agreement No. 824135 (project SOLARNET). A.V. is supported by NASA grant 80NSSC19K1261.

ORCID iDs

Anatoly Belov https://orcid.org/0000-0002-1834-3285
Athanasios Papaioannou https://orcid.org/0000-0002-9479-8644
Maria Abunina https://orcid.org/0000-0002-2152-6541
Mateja Dumbovic https://orcid.org/0000-0002-8680-8267
Ian G. Richardson https://orcid.org/0000-0002-3855-3634
Bernd Heber https://orcid.org/0000-0003-0960-5658
Patrick Kuhl https://orcid.org/0000-0002-3758-9272
Konstantin Herbst https://orcid.org/0000-0001-5622-4829
Anastasios Anastasiadis https://orcid.org/0000-0002-5162-8821
Angelos Vourlidas https://orcid.org/0000-0002-8164-5948
Eugenia Eroshenko https://orcid.org/0000-0003-3308-993X
Artem Abunin https://orcid.org/0000-0003-1427-3045

References

Adriani, O., Barbarino, G. C., Bazilevskaja, G. A., et al. 2009, NuPhS, 188, 296
Aguilar, M., Aisa, D., Alpat, B., et al. 2015, PhRvL, 115, 211101
Asipenka, A. S., Belov, A. V., Eroshenko, E. A., et al. 2009, AdSpR, 43, 708
Belov, A. 2000, SSRv, 93, 79
Belov, A., Abunin, A., Abunina, M., et al. 2015, SoPh, 290, 1429
Belov, A., Eroshenko, E., Yanke, V., et al. 2018, SoPh, 293, 68
Belov, A. V. 2009, in IAU Symp. 257, Universal Heliophysical Processes, ed. N. Gopalswamy & D. F. Webb (Cambridge: Cambridge Univ. Press), 439
Belov, A. V., Eroshenko, E. A., Oleneva, V. A., Struminsky, A. B., & Yanke, V. G. 2001, AdSpR, 27, 625
Berdichevsky, D., Bougeret, J.-L., Delaboudinière, J.-P., et al. 1998, GeoRL, 25, 2473
Blanco, J. J., Hidalgo, M. A., Gómez-Herrero, R., et al. 2013, A&A, 556, A146
Cane, H. V. 1993, JGR, 98, 3509
Cane, H. V. 2000, SSRv, 93, 55
Cane, H. V., Richardson, I. G., & St Cyr, O. C. 1998, GeoRL, 25, 2517
Cane, H. V., Richardson, I. G., & St Cyr, O. C. 2000, GeoRL, 27, 3591
Cane, H. V., Richardson, I. G., & von Rosenvinge, T. T. 1993, JGR, 98, 13295
Cane, H. V., Richardson, I. G., & von Rosenvinge, T. T. 2010, JGRA, 115, A08101
Cane, H. V., Richardson, I. G., von Rosenvinge, T. T., & Wibberenz, G. 1994, JGR, 99, 21429
Cane, H. V., Richardson, I. G., & Wibberenz, G. 1995, Proc. ICRC (Rome), 4, 377
Cane, H. V., Richardson, I. G., & Wibberenz, G. 1997, JGR, 102, 7075
Consolandi, C. & AMS Collaboration 2015, Proc. ICRC (The Hague), 34, 117
Duldig, M. L., & Humble, J. E. 1992, PASAu, 10, 24
Dumbović, M., Heber, B., Vršnak, B., Temmer, M., & Kirin, A. 2018, ApJ, 860, 71
Dumbović, M., Vršnak, B., Čalogović, J., & Župan, R. 2012, A&A, 538, A28
Dumbović, M., Vršnak, B., Guo, J., et al. 2020, SoPh, 295, 104
Dunzlaff, P., Heber, B., Kopp, A., et al. 2008, AnGeo, 26, 3127
Forbush, S. 1938, TeMAE, 43, 203
Freiherr von Forstner, J. L., Guo, J., Wimmer-Schweingruber, R. F., et al. 2020, JGRA, 125, e27662
Gopalswamy, N., Akiyama, S., Yashiro, S., et al. 2015, arXiv:1508.01603
Guo, J., Lillis, R., Wimmer-Schweingruber, R. F., et al. 2018, A&A, 611, A79
Gushchina, R. T., Belov, A. V., Obridko, V. N., & Shelting, B. D. 2012, Ge&Ae, 52, 438
Gushchina, R. T., Belov, A. V., & Yanke, V. G. 2013, JPhCS, 409, 012169
Heber, B., Wallmann, C., Galsdorf, D., et al. 2015, CEAB, 39, 75
Hess, V. F., & Demmelmair, A. 1937, Natur, 140, 316
Jokipii, J. R. 1971, RvGSP, 9, 27
Jordan, A. P., Spence, H. E., Blake, J. B., & Shaul, D. N. A. 2011, JGRA, 116, A11103
Kadokura, A., & Nishida, A. 1986, JGR, 91, 13
Klein, L. W., & Burlaga, L. F. 1982, JGR, 87, 613
Klyueva, A., Belov, A., & Eroshenko, E. 2017, Ge&Ae, 57, 177
Kühl, P., Banjac, S., Heber, B., et al. 2015, CEAB, 39, 119
Kühl, P., Dresing, N., Heber, B., & Klassen, A. 2017, SoPh, 292, 10
Kühl, P., Gómez-Herrero, R., & Heber, B. 2016, SoPh, 291, 965
Kühl, P., & Heber, B. 2019, SpWea, 17, 84
Kunow, H., Dröge, W., Heber, B., et al. 1995, SSRv, 72, 397
Light, C., Bindi, V., Consolandi, C., et al. 2020, ApJ, 896, 133
Lockwood, J. A. 1971, SSRv, 12, 658
Lockwood, J. A., Webber, W. R., & Debrunner, H. 1991, JGR, 96, 5447
Masías-Meza, J. J., Dasso, S., Démoulin, P., Rodriguez, L., & Janvier, M. 2016, A&A, 592, A118
McCracken, K. G., Beer, J., Steinhilber, F., & Abreu, J. 2013, SoPh, 286, 609

McCracken, K. G., Rao, U. R., & Bukata, R. P. 1966, PhRvL, 17, 928
Melkumyan, A. A., Belov, A. V., Abunina, M. A., et al. 2019, AdSpR, 63, 1100
Monk, A. T., & Compton, A. H. 1939, RvMP, 11, 173
Moraal, H., Belov, A., & Clem, J. M. 2000, SSRv, 93, 285
Müller-Mellin, R., Kunow, H., Fleißner, V., et al. 1995, SoPh, 162, 483
Munakata, K., Yasue, S., Kato, C., et al. 2006, AdG, 2, 115
Munini, R., Boezio, M., Bruno, A., et al. 2018, ApJ, 853, 76
Nishida, A. 1983, JGR, 88, 785
Okike, O. 2020, MNRAS, 491, 3793
Owens, M. J. 2006, JGRA, 111, A12109
Owens, M. J., & Forsyth, R. J. 2013, LRSP, 10, 5
Paizis, C., Heber, B., Ferrando, P., et al. 1999, JGR, 104, 28241
Papaioannou, A., Belov, A., Abunina, M., et al. 2019, SoPh, 294, 66
Papaioannou, A., Belov, A., Abunina, M., et al. 2020, ApJ, 890, 101
Papaioannou, A., Malandraki, O., Belov, A., et al. 2010, SoPh, 266, 181
Papaioannou, A., Sandberg, I., Anastasiadis, A., et al. 2016, JSWSC, 6, A42
Parker, E. N. 1958, ApJ, 128, 664
Parker, E. N. 1965, SSRv, 4, 666
Paularena, K. I., Wang, C., von Steiger, R., & Heber, B. 2001, GeoRL, 28, 2755
Potgieter, M. S. 2013, LRSP, 10, 3
Richardson, I. G. 1997, GMS, 99, 189
Richardson, I. G. 2004, SSRv, 111, 267
Richardson, I. G. 2018, LRSP, 15, 1
Richardson, I. G., & Cane, H. V. 2010, SoPh, 264, 189
Richardson, I. G., & Cane, H. V. 2011, SoPh, 270, 609
Roussos, E., Jackman, C. M., Thomsen, M. F., et al. 2018, Icar, 300, 47
Sanderson, R. T., Beeck, J., Marsden, G. R., et al. 1990, Proc. ICRC (Adelaide), 6, 255
Simpson, J. A., Anglin, J. D., Balogh, A., et al. 1992, A&AS, 92, 365
Thomas, S. R., Owens, M. J., & Lockwood, M. 2014, SoPh, 289, 407
Webb, D. F., Lepping, R. P., Burlaga, L. F., et al. 2000, JGR, 105, 27251
Webber, W. R., Cummings, A. C., McDonald, F. B., et al. 2007, GeoRL, 34, L20107
Wibberenz, G., Le Roux, J. A., Potgieter, M. S., & Bieber, J. W. 1998, SSRv, 83, 309
Winslow, R. M., Schwadron, N. A., Lugaz, N., et al. 2018, ApJ, 856, 139
Witasse, O., Sánchez-Cano, B., Mays, M. L., et al. 2017, JGRA, 122, 7865